
Observations of Modulated Shock Waves in Solid Targets Driven by Spatially Modulated Laser Beams

Introduction

Shock waves produced by laser-driven ablation are an important part of studies of inertial confinement fusion (ICF),^{1,2} the equation of state of materials (EOS),^{3–5} laboratory astrophysics,^{6,7} and other high-energy-density sciences. In ICF, nonuniformities in the drive laser can produce nonuniform shocks that create mass perturbations in the target.² These perturbations can be amplified by the Rayleigh–Taylor (RT)¹ instability to a sufficiently large enough level to disrupt the implosion and reduce its performance. The propagation of these modulated shocks is determined by the physics of the laser-interaction region and stabilization processes;^{8,9} hence, their measurement provides information about the intervening processes. Modulations in drive intensity can also be used to verify the scaling of shock strength (velocity) with drive intensity to better understand coupling efficiency and its scaling with intensity.

This article reports on novel experiments in which targets are driven with a laser beam having a single-mode, spatial-intensity modulation. The resultant ablation-pressure modulations produce shocks with spatially varying strengths (and velocities). The arrival times of the shock at various surfaces in the target are used to infer differences in the shock velocities and therefore the pressures produced by the modulated drive intensity. By placing an embedded layer within the target, the shock arrival at two surfaces is measured, thereby providing an added opportunity to observe the evolution of the modulated shock as it traverses the target. This evolution can be used to study dynamic effects in laser-produced plasmas, namely stabilization by dynamic overpressure.⁹

Experimental Results

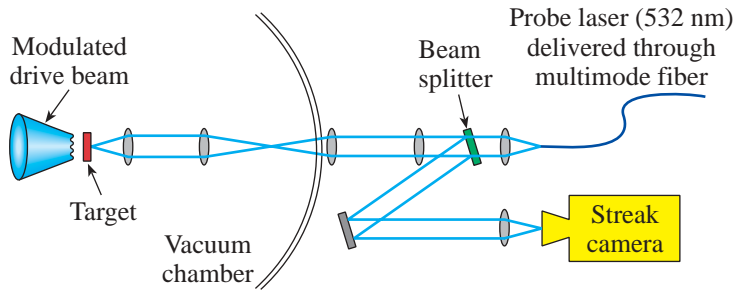
In these experiments, 20- μm -thick CH ($\rho = 0.92 \text{ g/cm}^3$) targets were irradiated with 351-nm laser light at average intensities of $6 \times 10^{12} \text{ W/cm}^2$. A 0.5- μm -thick Al layer was embedded at the center (10 μm deep) of the target. This layer provided an intermediate surface where the shock arrival was detected. Modulations in drive intensity of $\sim 5:1$ produced $\sim 3:1$ modulations in shock pressure. Hydrodynamic simulation of

these experiments is in good agreement with the average shock speeds, their modulations, and the resultant breakout times.

These experiments were conducted on the OMEGA¹⁰ laser using a single drive beam having a distributed phase plate (DPP)¹¹ that produces a modulated intensity pattern at its focal spot. The phase plate was designed and fabricated to produce a one-dimensional irradiance distribution on a flat target placed in the quasi far field of the OMEGA laser beam. One-quarter of the Talbot cycle (the transition from only phase modulation to only intensity modulation) was used to achieve a sinusoidal irradiance distribution, with flat phase, from a sinusoidal phase distribution, with flat irradiance, in the near field of the laser. Photolithographic and ion-etching techniques were used to place a surface relief in fused silica.¹¹ As the laser beam traverses the etched-glass plate, it acquires the needed phase distribution from the etched pattern to produce a sinusoidal intensity distribution at the focal plane. The focusing lens was positioned to obtain a spatial wavelength of 60 μm at the target plane.

This beam was incident on the target at an angle of 23°. The modulations were oriented so that obliquity distortions were negligible in the modulation direction. The arrival of the shock front at the rear and embedded surfaces was detected using the active-shock-breakout (ASBO) diagnostic.¹² It uses a 532-nm (doubled Nd:YAG) probe laser directed onto the back of the experimental targets to detect shock velocity or breakout times.

Figure 90.18 shows the experimental arrangement with the UV drive laser incident from the left onto the front of the target and the ASBO probe laser incident from the right, probing the rear side of the target. The ASBO diagnostic normally uses the time-resolved displacement of VISAR (velocity interferometer system for any reflector) fringes^{12,13} to detect shock velocity. In the case of opaque materials, the ASBO probe beam does not detect the shock wave within the material but records the disruption of the rear-surface reflectivity produced there by the arrival of the shock. (The release of the rear surface



E11493

produces an expanding plume of material that quickly absorbs the laser energy.) The shock speeds are deduced from the known material thickness and the shock transit time as measured by this breakout.

Figure 90.19(a) shows an optical image of the drive-laser intensity distribution obtained with a charge-coupled-device (CCD) camera placed at an equivalent target plane¹⁴ for the OMEGA laser. The distributed phase plate described above produced the modulations in the laser focal spot. The focal position was chosen to produce modulations with a wavelength of $\sim 60 \mu\text{m}$; the resultant spot was about $800 \mu\text{m}$ in diameter.

Figure 90.19(b) is a plot of the intensity distribution in the vertical direction along the center of the image. The intensity modulations range between 5:1 and 3:1, depending on which area of the focal spot is analyzed. This variation occurs because the nonuniformities in phase and irradiance of the laser beam are comparable to those that produce the sinusoidal pattern. (These effects can be compensated for in future designs.) The absolute values for the on-target intensity were obtained by normalizing the total distribution of intensities to the incident laser power for shot 24569.

Figure 90.20 is a pinhole-camera image of the x rays emitted from an Au target irradiated by this beam [Fig. 90.19(a)] at an average intensity of $\sim 10^{14} \text{ W/cm}^2$. This intensity is higher than that used to drive the targets but is used to produce sufficient x rays for imaging purposes. At this intensity the x rays are predominately from *n*-shell Au emission. The lower apparent modulation amplitude results from the nonlinear conversion of the UV to x-ray energy.

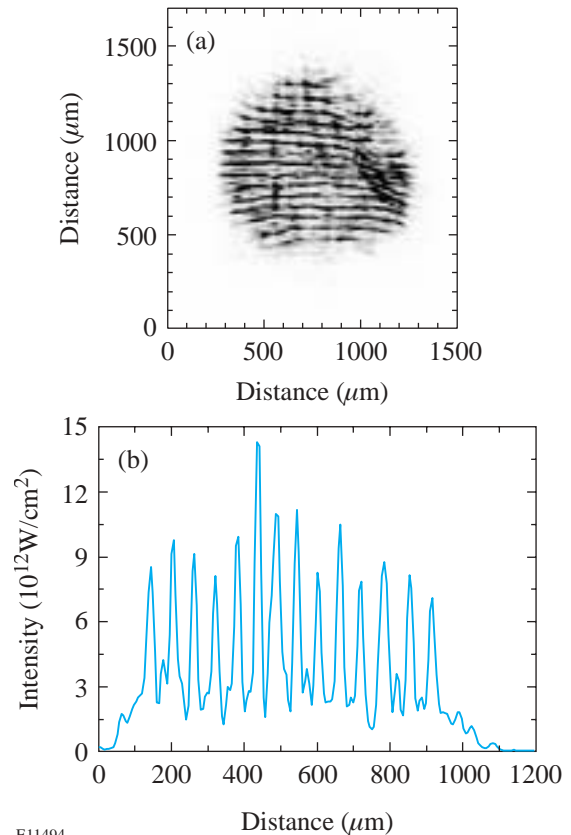
The opaque layer ($0.5 \mu\text{m}$ of Al) embedded in the target provides an internal surface at which the shock arrival is detected. The depth of that imbedded layer was $10 \mu\text{m}$ from the irradiated surface; another $10 \mu\text{m}$ of CH was coated on the rear

Figure 90.18

The experimental arrangement in the OMEGA target chamber. The UV drive laser is incident from the left, and the green probe beam is incident from the right. The incident beam has a DPP that produces sinusoidal intensity modulations at the focal plane. The reflected probe beam is directed to an optical streak camera.

side. The heat front did not penetrate the front $10 \mu\text{m}$ of CH to the Al layer while the laser was on.

Figure 90.21 shows the time-resolved ASBO data for two shots, depicting the signal reflected from targets irradiated by the intensity distribution shown in Fig. 90.19. (The series of

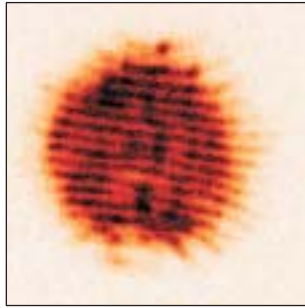


E11494

Figure 90.19

(a) An optical image at an equivalent target plane for the OMEGA laser. These modulations in drive intensity are created by a DPP placed in the beam and are used to create modulated shocks in the target. (b) A lineout of intensity along the centerline of the image.

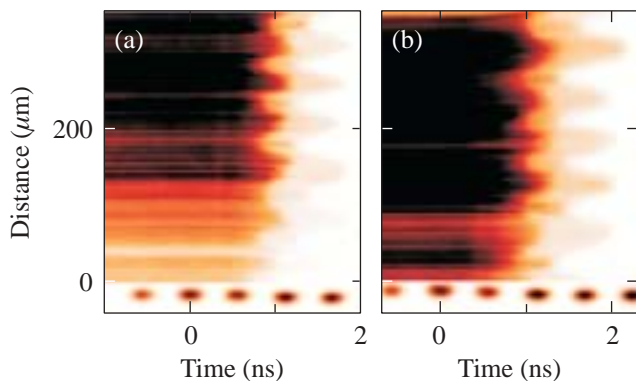
dots across the bottom of the figures are temporal fiducial pulses, each separated by 0.548 ns.) For these experiments, one leg of the VISAR interferometer was blocked, producing a simple probe beam, giving a continuous spatial record of the shock-breakout time. The ASBO probe beam penetrates the rear portion of the target ($10\ \mu\text{m}$ of transparent CH) and reflects



E11495

Figure 90.20

An x-ray pinhole-camera image of the x rays emitted from a Au target irradiated by the beam shown in Fig. 90.19(a).



E11496

Figure 90.21

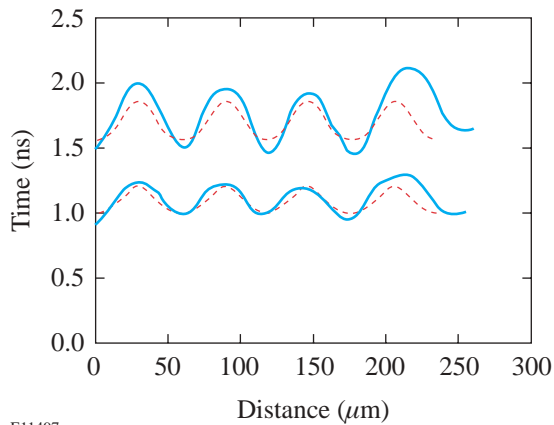
Streak records of probe beam reflection from (a) shot 24566 and (b) shot 24569. The dark signal from approximately $-1\ \text{ns}$ to $+1\ \text{ns}$ is the probe beam reflection off the unshocked Al layer within the target. The transition to the lighter area occurs when the shock arrives at the Al layer, reducing its reflectivity. The cessation of that light area (later in time) is caused by the arrival of the shock at the rear surface. The modulations in each of these transition regions result from different arrival times of the modulated shock in the target.

off the embedded Al layer. This reflection is seen as the dark portion of the image that extends from less than -1 to $\sim 1\ \text{ns}$. (The horizontal streaks seen in these signals are due to the spatial speckle of the probe laser.) The drive laser began at $0\ \text{ns}$. At about $+1\ \text{ns}$, the shock arrives at the Al layer and changes the layer's reflectivity, signaling the arrival of the shock at that surface. At that point, the signal to ASBO decreases but does not completely disappear. This reduction in signal results from either reduced reflectivity of the Al or reduced transmissivity of the rear CH section. Both are caused by the shock's arrival at the Al layer. The contour of change in reflectivity (dark to light transition) is modulated at the same spatial frequency as the incident laser modulations. The earlier occurrences of this transition represent the arrival of faster portions of the shock (shorter transit times) and later occurrences the slower portions (longer transit times). The lighter region persists until about 1.5 to $2\ \text{ns}$, then it disappears completely. This total loss of signal occurs when the shock arrives at the rear surface and that surface unloads, no longer reflecting the probe laser. Note that the extinction time of this light area is also modulated and it is in phase with the dark-to-light transition at $\sim 1\ \text{ns}$. These transitions in target reflectivity mark the arrival of the shock front at each surface and can therefore be used to infer shock velocities and modulations in those velocities.

Analysis

Figure 90.22 shows a plot (solid curves) of the shock arrival times (at the Al layer and the rear surface) as a function of space as deduced from Fig. 90.21(b). Using these data and the thickness of the intervening target material, the shock speed as a function of space can be inferred. In the lower curve, the earliest times (corresponding to intensity peaks) occur at $\sim 0.97\ \text{ns}$, and the latest times (intensity troughs) occur at $\sim 1.15\ \text{ns}$. The respective times for the upper curves are $1.47\ \text{ns}$ and $1.95\ \text{ns}$, where $t = 0$ is the start of the laser pulse. Each of these values represents the average of three peaks or troughs. (The trend to later times at the right end of these plots likely results from the finite size of the laser spot. Its edges have slightly lower intensity and hence produce slower shocks that arrive at the surfaces later in time.) Using the $10\text{-}\mu\text{m}$ distance for transit times at the peak and trough of the modulated shock, we find that the minimum shock speed is $12.5\ \mu\text{m}/\text{ns}$ and the maximum is $20\ \mu\text{m}/\text{ns}$. The errors in velocity are expected to be $\leq 5\%$ and arise mainly from uncertainties in target thickness ($\pm 0.1\ \mu\text{m}$) and determination of shock arrival time ($\sim \pm 10\ \text{ps}$). Using the Hugoniot data for CH from *SESAME* tables,¹⁵ these shock velocities correspond to pressures of 2.85 and $0.97\ \text{Mb}$, respectively. In a similar shot with an identical target, the

shock speeds were slightly higher but the modulations of similar size. Table 90.III lists the results for the two shots. The breakout times (t_P and t_T for peaks and troughs) at either $10\ \mu\text{m}$ or $20\ \mu\text{m}$ in the target were averaged over three spatial periods. V_- is the shock velocity given by the distance ($10\ \mu\text{m}$) divided by the difference between later breakout times (troughs of shock); V_+ is the velocity associated with the earlier breakout times (peaks of shock). The pressures P_- and P_+ are inferred from the shock velocities V_- and V_+ using the *SESAME* equation-of-state tables. I_+/I_- is the ratio of intensity calculated from the pressure ratio P_+/P_- using the intensity scaling for pressure as given below.



E11497

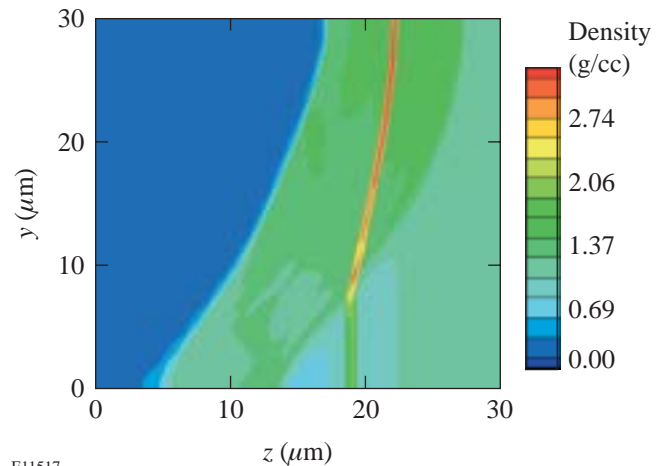
Figure 90.22

The shock arrival times versus space for shot 24566 [Fig. 90.21(b)]. The upper curve represents the contour of the shock arrival time at the rear surface; the lower curve for the arrival at the Al layer embedded at $10\ \mu\text{m}$. The dashed lines are the simulated arrival times of the shock at those surfaces.

The dependence of pressure on intensity has been established by considerable ICF research as $P(\text{Mbar}) = 40 (I/\lambda)^{2/3}$ (Refs. 16–18), where λ is the laser wavelength in μm and I is laser intensity in $10^{15}\ \text{W}/\text{cm}^2$. It is expected that for the intensities in these experiments, plasma instabilities are not important and this scaling law should be valid. At $6 \times 10^{12}\ \text{W}/\text{cm}^2$, the pressure should be $\sim 2.7\ \text{Mb}$; a factor-of-5

reduction in intensity should produce a 0.9-Mb shock. These numbers are in good agreement with the observed pressure changes as inferred from the modulations in shock velocity, as shown in Table 90.III. Note that the pressure modulations are similar for the two shots, despite the differences in absolute pressure. This is because the sinusoidal intensity distribution was the same for both shots. The absolute pressure is different because the laser power (pulse shape and laser energy) was different (by a factor of ~ 5) for the two shots: $6 \times 10^{12}\ \text{W}/\text{cm}^2$ and $1.5 \times 10^{12}\ \text{W}/\text{cm}^2$.

Figure 90.23 shows a contour plot depicting density from a 2-D hydrodynamic simulation of this experiment using the computer code *ORCHID*.¹⁹ The laser is incident from the left, and the shock (propagating to the right) can be seen as the first contour. A portion of the embedded Al layer (indicated in the figure) has been displaced by the shock. The laser intensity was $6 \times 10^{12}\ \text{W}/\text{cm}^2$ (average) in a sinusoidal intensity distribution with $60\text{-}\mu\text{m}$ wavelength and intensity modulation (peak-to-



E11517

Figure 90.23

Density contours (at 1.39 ns) in a 2-D hydrocode (*ORCHID*) simulation of these experiments with an embedded Al layer as shown. The modulated laser (1/2 cycle of the sinusoidal modulation is shown) is incident from the left. The curved shock propagates to the right.

Table 90.III: Experimental results.

Shot #	(W/cm ²)	Trough		Peak		Velocity		Pressure		Modulation	
		t_{T20}	t_{T10}	t_{P20}	t_{P10}	V_-	V_+	P_-	P_+	P_+/P_-	I_+/I_-
24566	6×10^{12}	1.62	1.06	1.15	0.813	17.8	29.6	2.18	6.45	2.96	5.09
24569	1.4×10^{12}	1.95	1.15	1.47	0.973	12.5	20.1	0.97	2.85	2.94	5.04

valley) of 5:1. The predicted arrival time of the shock at the embedded layer and the rear surface is shown as dashed curves in Fig. 90.22.

Conclusion

These experiments have demonstrated a technique for observing modulated shocks in solid targets. Modulations in the drive intensity produce shocks with spatially varying speeds. The arrival of these shocks at surfaces of the target was detected with an optical probe beam. The transit times of the shocks through the targets provide the velocities at various points along the shock front and detect the modulations in shock velocity. These velocities were used to infer the resultant pressure modulations produced by modulations in drive intensity. The experimental results are consistent with established models for the intensity scaling of ablation pressure. The 2-D hydrocode *ORCHID* modeled the observed breakout times and modulations accurately. This technique will be useful for studying dynamic overpressure where ablation dynamics may alter the amplitude of shock modulations as it propagates through a target. In addition, these results confirm established scaling laws for ablation pressure with drive intensity.

ACKNOWLEDGMENT

This work was supported by the U.S. Department of Energy Office of Inertial Confinement Fusion under Cooperative Agreement No. DE-FC03-92SF19460, the University of Rochester, and the New York State Energy Research and Development Authority. The support of DOE does not constitute an endorsement by DOE of the views expressed in this article.

REFERENCES

1. J. D. Lindl, *Phys. Plasmas* **2**, 3933 (1995).
2. S. E. Bodner, D. G. Colombant, J. H. Gardner, R. H. Lehberg, S. P. Obenschain, L. Phillips, A. J. Schmitt, J. D. Sethian, R. L. McCrory, W. Seka, C. P. Verdon, J. P. Knauer, B. B. Afeyan, and H. T. Powell, *Phys. Plasmas* **5**, 1901 (1998).
3. G. W. Collins *et al.*, *Science* **281**, 1178 (1998).
4. R. Cauble *et al.*, *Phys. Plasmas* **4**, 1857 (1997).
5. G. W. Collins *et al.*, *Phys. Plasmas* **5**, 1864 (1998).
6. B. A. Remington *et al.*, *Science* **284**, 1488 (1999).
7. B. A. Remington *et al.*, *Phys. Plasmas* **7**, 1641 (2000).
8. V. N. Goncharov, "Self-Consistent Stability Analysis of Ablation Fronts in Inertial Confinement Fusion," Ph.D. thesis, University of Rochester, 1998.
9. V. N. Goncharov, S. Skupsky, T. R. Boehly, J. P. Knauer, P. McKenty, V. A. Smalyuk, R. P. J. Town, O. V. Gotchev, R. Betti, and D. D. Meyerhofer, *Phys. Plasmas* **7**, 2062 (2000).
10. T. R. Boehly, D. L. Brown, R. S. Craxton, R. L. Keck, J. P. Knauer, J. H. Kelly, T. J. Kessler, S. A. Kumpan, S. J. Loucks, S. A. Letzring, F. J. Marshall, R. L. McCrory, S. F. B. Morse, W. Seka, J. M. Soures, and C. P. Verdon, *Opt. Commun.* **133**, 495 (1997).
11. T. J. Kessler, Y. Lin, J. J. Armstrong, and B. Velazquez, in *Laser Coherence Control: Technology and Applications*, edited by H. T. Powell and T. J. Kessler (SPIE, Bellingham, WA, 1993), Vol. 1870, pp. 95–104.
12. P. M. Celliers *et al.*, *Appl. Phys. Lett.* **73**, 1320 (1998).
13. L. M. Barker and R. E. Hollenbach, *J. Appl. Phys.* **43**, 4669 (1972).
14. S. P. Regan, J. A. Marozas, J. H. Kelly, T. R. Boehly, W. R. Donaldson, P. A. Jaanimagi, R. L. Keck, T. J. Kessler, D. D. Meyerhofer, W. Seka, S. Skupsky, and V. A. Smalyuk, *J. Opt. Soc. Am. B* **17**, 1483 (2000).
15. B. I. Bennett *et al.*, Los Alamos National Laboratory, Report LA-7130 (1978).
16. C. E. Max, *Physics of Laser Fusion, Vol. 1*, Lawrence Livermore National Laboratory, Livermore, CA, UCRL-53107, Rev. 1 (1982).
17. W. M. Manheimer, D. G. Colombant, and J. H. Gardner, *Phys. Fluids* **25**, 1644 (1982).
18. S. M. Pollaine and J. D. Lindl, *Nucl. Fusion* **26**, 1719 (1986).
19. R. L. McCrory and C. P. Verdon, in *Inertial Confinement Fusion*, edited by A. Caruso and E. Sindoni (Editrice Compositori, Bologna, Italy, 1989), pp. 83–124.